AGU PUBLICATIONS

JGR

Journal of Geophysical Research: Atmospheres

RESEARCH ARTICLE
10.1002/2015JD023564

Measuring black carbon spectral extinction in the visible and infrared

A. J. A. Smith[1], D. M. Peters[1,2], R. McPheat[2], S. Lukanihins[1], and R. G. Grainger[1]

[1] Atmospheric, Oceanic and Planetary Physics, Clarendon Laboratory, University of Oxford, Oxford, UK, [2] Molecular Spectroscopy Facility, Rutherford Appleton Laboratory, Harwell, UK

Key Points:
- A Mini-CAST soot generator was used to measure the properties of black carbon
- Extinction cross sections are calculated in the visible and near IR

Correspondence to:
A. J. A. Smith,
smith@atm.ox.ac.uk

Citation:
Smith, A. J. A., D. M. Peters, R. McPheat, S. Lukanihins, and R. G. Grainger (2015), Measuring black carbon spectral extinction in the visible and infrared, *J. Geophys. Res. Atmos.*, *120*, 9670–9683, doi:10.1002/2015JD023564.

Received 21 APR 2015
Accepted 31 AUG 2015
Accepted article online 5 SEP 2015
Published online 30 SEP 2015

Abstract This work presents measurements of the spectral extinction of black carbon aerosol from 400 nm to 15 μm. The aerosol was generated using a Miniature Combustion Aerosol Standard soot generator and then allowed to circulate in an aerosol cell where its extinction was measured using a grating spectrometer in the visible and a Fourier transform spectrometer in the infrared. Size distribution, number concentration, and mass extinction cross sections have also been obtained using single-particle aerosol samplers. A mean mass extinction cross section at 550 nm of 8.3 ± 1.6 m^2 g^{-1} is found which, assuming a reasonable single scatter albedo of 0.2, corresponds to a mass absorption cross section of 6.6 ± 1.3 m^2 g^{-1}. This compares well with previously reported literature values. Computer analysis of electron microscope images of the particles provides independent confirmation of the size distribution as well as fractal parameters of the black carbon aerosol. The aerosol properties presented in this work are representative of very fresh, uncoated black carbon aerosol. After atmospheric processing of such aerosols (which could include mixing with other constituents and structural changes), different optical properties would be expected.

1. Introduction

1.1. Black Carbon

Black carbon (BC) is one of the major particulate products of incomplete combustion, and one of the least well-understood contributors to positive anthropogenic radiative forcing [*Intergovernmental Panel on Climate Change (IPCC)*, 2013]. This is due, in part, to uncertainty in its spectral light scattering and absorption properties [*Bond et al.*, 2013]. Unlike the majority of atmospheric aerosols, BC has high absorption at solar wavelengths leading to a positive direct effect on radiative forcing [*Jacobson*, 2001; *Bond*, 2007; *Bahadur et al.*, 2011; *Bond et al.*, 2013; *IPCC*, 2013]. Over the last century, emission rates have increased dramatically [*Ito and Penner*, 2005; *Bond et al.*, 2007] with the majority of increases coming from transport and industry sources [*Bond et al.*, 2013]. However, changes in emissions have not been geographically uniform: while North America and Europe dominated early emissions, in the later half of the twentieth century, Asia has become the main emitter [*Bond et al.*, 2007].

Compounding the direct effect, absorbing aerosols reduce cloud cover by warming the atmosphere and so increasing evaporation [e.g., *Hansen et al.*, 1997]. Several works suggest that the surface albedo of snow is lowered by BC deposition, leading to additional warming [e.g., *Flanner et al.*, 2009; *Doherty et al.*, 2010]. There is also the issue of public health concerns [*Jansen et al.*, 2005] and poor urban visibility [*Larson et al.*, 1989]. The current best estimate of the net anthropogenic radiative forcing from BC emissions is 1.1 W m^2 [*Bond et al.*, 2013].

Black carbon fractal aggregate (BCFA) aerosols are created as a by-product of incomplete combustion. The processes involved are as follows:

1. Partially oxidized, vaporized fuel nucleates generating what are initially very small spherical particles with diameters of 1–2 nm.
2. These particles grow to diameters of up to 30 nm by coagulation [*Calcote*, 1981]. For a specific set of burning conditions, the sizes of these individual "spherules" cover a limited size range [*Vander Wal et al.*, 1999].
3. While leaving the flame, these spherules collide and combine, forming aggregate aerosols.

In this work, BC aerosol was generated using a laminar propane flame; however, it has been noted that the BC particles "formed in various combustion processes are rather similar" [*Wagner*, 1981]. Diesel fuels tend

to create BCFAs with smaller spherules than those from other fuels, particularly in more modern engines [*Su et al.*, 2004]. Additionally, the chain lengths and fractal dimensions of these aggregates can alter with the fuel burnt [*Köylü and Faeth*, 1992], but overall, the variability in microphysical properties between various fresh BC aerosols is not large in practice. Additionally, *Moore et al.* [2014] found that the range of soots created by the Miniature Combustion Aerosol Standard (Mini-CAST) overlapped well with reported aircraft and diesel engine emissions.

In normal atmospheric conditions, the time taken for these aggregate particles to collapse into more compact structures [*Martins et al.*, 1998a] is of the order of hours [*Martins et al.*, 1998b]. Despite BC spherules being hydrophobic, the irregular shapes of BCFAs permit sites for water deposition. This leads to coating by other hydrophilic materials [*Popovicheva et al.*, 2008; *Zhang et al.*, 2008]. The coatings increase the light absorption of the aerosols [*Fuller et al.*, 1999; *Bond et al.*, 2006].

In this work, the BC measured was extremely fresh, with around a 25 min gap between initial creation of the aerosol and measurement. As such, the particles described in this section are not expected to be coated or collapsed as they would have had very little opportunity for atmospheric processing.

1.2. Specific Cross Sections—Background and Previous Measurements

When quantifying the impact of BC aerosol on climate, the most relevant optical parameters are the mass absorption cross section (MAC) and the single scatter albedo, ω_0. Following the excellent review of *Moosmüller et al.* [2009], the measurement of aerosol absorption can be categorized into three broad types.

The first of these types are filter methods in which aerosol is collected upon a filter and then transmission through the filter measured. Various techniques can be applied to account for the light that has not been transmitted through the filter due to scattering instead of absorption, and the enhancement due to interaction of light between particles and the filter. Second are methods using in situ thermal techniques to irradiate the aerosol, increasing its temperature. A property resulting from this heating is measured. The most popular of these methods are (a) the photoacoustic technique in which the heated particle transfers this heat to the surrounding air, causing a sound wave which can be detected, and (b) incandescence techniques, a prominent example being the Single-Particle Soot Photometer which uses a laser to heat particles to very high temperatures such that their thermal emission or incandescence can be detected at visible wavelengths. The final types are extinction and scattering measurements. Here the absorption is obtained by subtracting the scattered light from the total light extinction. An example of extinction and scattering techniques is the combination of cavity ring-down extinction measurements with reciprocal nephelometry to capture scattered light. For further details of these techniques the reader is directed to *Moosmüller et al.* [2009, and references therein].

The method described in this work obtains the extinction of BC aerosol. However, as the wavelength of light increases to the infrared (IR), theoretical calculations of BC fractal light scatterers show that ω_0 approaches 0 [*Smith and Grainger*, 2014] and so absorption and extinction are very similar. As reported values of single scatter albedo at 550 nm are in the range $0.15 < \omega_0 < 0.29$ [see *Bond and Bergstrom*, 2006, Table 7] it is not safe to make this assumption at short wavelengths. Future work will present retrievals of BC aerosol refractive index using the method of *Thomas et al.* [2005] which leads to ω_0 as a derived parameter of the retrieval.

1.3. Fractal Aggregate Particles

Fractal aggregate particles are often described using very different variables from those used for more spherical particles. In order to calculate the fractal and microphysical properties of the particles from electron microscopy images, it is necessary to introduce these concepts here. Obtaining the size distributions of particles from these images is also a useful validation of measurements from other aerosol sizing instruments which assume a more regular shape of particle.

The defining equation for fractal geometry of aggregates is

$$n_s = k_f \left(\frac{R_g}{a} \right)^{D_f}, \tag{1}$$

where n_s is the number of primary spherules in the aggregate, a is the radius of an individual spherule in the fractal, D_f is the fractal dimension, k_f is the fractal prefactor, and R_g is the radius of gyration giving the RMS distance of spherules from the cluster's center of mass [*Sorensen*, 2001]. If it were possible to measure n_s and R_g of particles, the value of D_f could be calculated from a linear fit of $\ln(n_s)$ versus $\ln(R_g)$. However, it is not

possible to obtain these parameters using a 2-D projection of the aggregates and so other methods, first proposed by *Köylü et al.* [1995], must be attempted.

First, the relationship between a projected area of an aggregate, A_a, and the number of primary spherules, n_s, is given by

$$n_s = k_a \left(\frac{A_a}{A_p} \right)^{\alpha}, \tag{2}$$

where A_p is the projected area of a primary spherule, k_a is a constant prefactor of order unity (different from k_f mentioned above), and α is an empirical scaling constant. Second is the relationship between the projected radius of gyration, R_g^{2D}, and the true value, R_g:

$$\frac{R_g}{R_g^{2D}} = \text{constant}. \tag{3}$$

This relationship provides a method of calculating R_g^{3D} from the measurable R_g^{2D}.

Under the assumption that primary particle size does not change, equations (2) and (3) can be substituted into equation (1). Taking the logarithms yields

$$\ln(A_a) = \frac{D_f}{\alpha} \ln(R_g^{2D}) + c, \tag{4}$$

where c is the value of some constant not of interest. If α can be determined, then D_f can be obtained from a linear fit to equation (4). In fact, any linear length scale will do instead of R_g^{2D} in equation (4). Following *Köylü et al.* [1995], for the remainder of this work, the geometric mean of minimum and maximum projected diameters, F_{mm}, will be used instead of R_g^{2D}.

2. Method

2.1. Experimental Setup

The main experiments were carried out at the Rutherford Appleton Laboratory's Molecular Spectroscopy Facility between 26 November and 4 December 2013. Soot was generated by burning propane and inserting the combustion products into a 75 L aerosol chamber for optical measurements. After leaving the aerosol chamber, the microphysical properties of the aerosol were measured using a suite of sizing and sampling instruments.

Seven measurements made of BC aerosol transmission were of suitable quality to obtain mass extinction cross sections (MEC). Data collected on 2 December 2013 were not usable in the IR due to insufficient particulate in the aerosol cell. This resulted in transmissions close to unity which were extremely noisy. On this day the visible wavelength data were still of sufficient quality due to the far greater absorption of BC at shorter wavelengths.

2.1.1. Soot Generation and the Aerosol Cell

Black carbon was generated using a Jing Aerosol Ltd. Mini-CAST 5201A soot generator. In this equipment, a coflow diffusion flame forms soot particles which are then removed from the flame without coming into contact with oxygen, by way of a nitrogen quenching gas which inhibits further combustion. Additional diluting gas reduces the aerosol concentration in the flow. By controlling the fuel, air, nitrogen quenching, and nitrogen dilution flow rates entering the Mini-CAST, it is possible to generate a repeatable soot aerosol. Adjustment of the quenching flow rate allows selection of modal diameters from 30 to 190 nm. Adjustment of the fuel to air ratio enables control of the soot's organic content. A full description of burning regimes available with the Mini-CAST can be found in *Moore et al.* [2014].

The C/O ratio is the number of carbon atoms relative to oxygen atoms available in the flame. This describes whether burning conditions are fuel rich (when, for propane, C/O> 0.3) so that there is not enough oxygen present for complete combustion or fuel lean so that the opposite holds [*Moore et al.*, 2014]. In the experiments carried out here, the C/O ratio was controlled by varying the amount of oxidation air provided to the Mini-CAST while holding all other gas flows constant.

The flow configuration from soot generation to removal from the aerosol measurement cell is shown in Figure 1. Mass flow controllers (MFC) were used to accurately control the input of gases into the Mini-CAST.

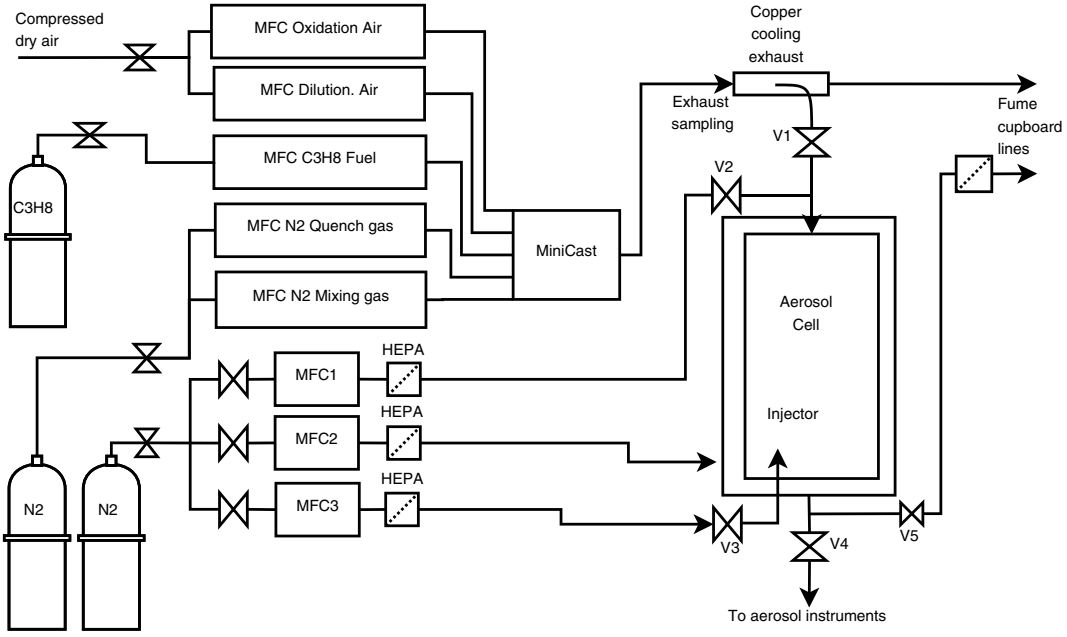

Figure 1. Experimental setup for loading of the aerosol cell with soot. The optical equipment mounted on the exterior of the aerosol cell is shown in Figure 3. Mass flow controllers are labeled MFC; bow tie symbols represent valves; dashed boxes represent aerosol filters used to scrub particulate from a flow.

After leaving the burner, the aerosol and exhaust gases are fed through a copper cooling exhaust and then some of this flow (as well as the carrying mixing gas) is fed into the aerosol cell. The compressed dry air used to provide oxygen to the flame is filtered and dehumidified.

Three additional MFCs are configured to add additional N_2 flows into the cell. MFC1 allows additional aerosol dilution. MFC2 provides a constant purge to the optics and windows at the sides of the cell stopping contamination of the optical elements by deposition of soot. MFC3 controls an upward facing jet nozzle at the bottom of the cell. The nozzle was selected to be sufficiently small, with flow rates high enough to generate turbulent jet flow into the cell providing uniform mixing of the aerosol.

During an experiment, valves V1 – V4 (and all unlabeled valves) would be open and V5 closed so that aerosol leaving the cell is fed to the aerosol instruments (shown in Figure 2) which draw a constant flow. By setting the total mass flow into the aerosol cell via MFC1 – MFC3 to be less than the aerosol instrument flow, an aerosol sample from the soot generator exhaust is drawn into the cell via V1. To purge the cell, the MFC1 – MFC3 flow rates are dramatically increased. A description of the aerosol instruments is provided in section 2.1.3.

The Mini-CAST was operated with constant flows of 0.06 standard liters per minute (sLpm) of propane, 7.48 sLpm of quenching N_2, 20 sLpm of mixing N_2, and no dilution air. The oxidation air was varied over the course of the experiments from 0.7 to 1.23 sLpm in order to change the C/O ratio of the fuel. The ratio can be obtained by dividing the flow of fuel, f_f, by the flow of oxidizing air, f_{air} [*Schnaiter et al.*, 2006]:

$$\mathrm{C/O} = 7.16 \times \frac{f_f}{f_{air}}, \tag{5}$$

so that the range of values resulting is $0.35 \leq \mathrm{C/O} \leq 0.61$. These settings were chosen so that our results could be compared to those of *Schnaiter et al.* [2006] and also means that as the C/O ratio increases, the fraction of elemental carbon aerosol decreases, being replaced by organic carbon aerosol.

2.1.2. Optical Measurements

In order to measure the aerosol optical properties over a large range of wavelengths, two separate systems are employed in the aerosol cell. These are shown in Figure 3 which shows a cross section of the aerosol cell from above.

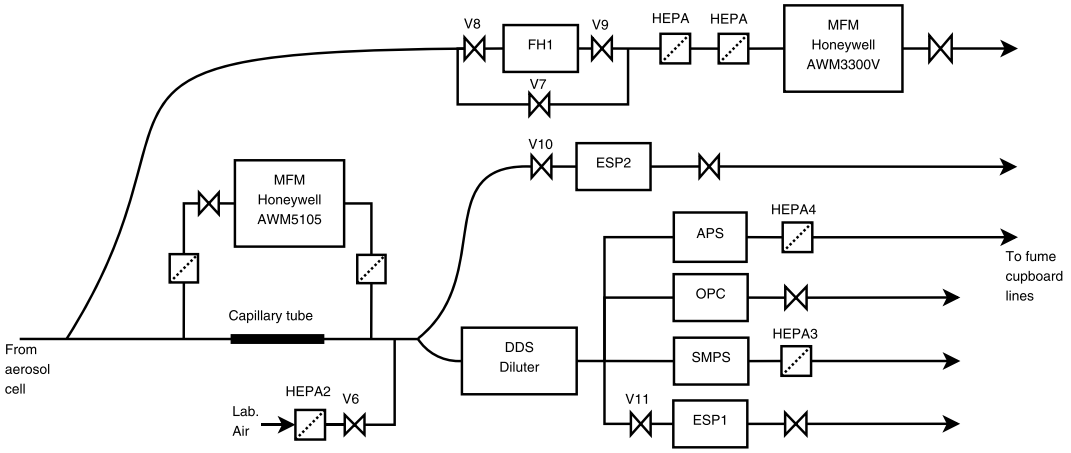

Figure 2. Experimental setup for aerosol microphysical measurements made downstream of the aerosol cell shown in Figure 1. A filter holder (FH1) was used to collect filter samples; electrostatic precipitators (ESP) were used to deposit individual particles onto stubs for subsequent analysis by electron microscopy and attenuated total reflection; mass flow meters (MFM) were used to monitor flow rates.

For visible wavelengths, a deuterium tungsten halogen source with a wavelength range of 215–2500 nm was coupled to a collimator and the light sent on a single pass through the cell. It was measured at the far end by an Ocean Optics S2000 CCD spectrometer. With this setup, the usable measurement range was $350 < \lambda < 870$ nm.

For the IR, a White cell was used with eight passes of either a globar or a halogen source. This was operating at 90° to the visible light path. A Bruker IFS-66 Fourier transform spectrometer (FTS) modulated the light before

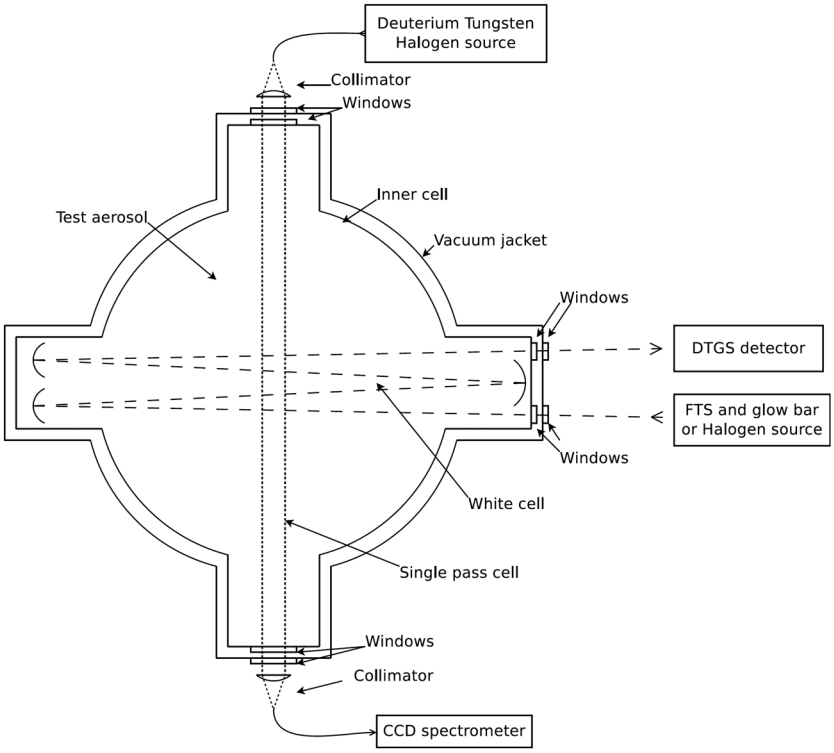

Figure 3. Optical setup of the aerosol cell. Visible range measurements were taken using the CCD spectrometer from a deuterium tungsten halogen source, with a single pass through the cell. Fourier transform spectrometer (FTS) measurements using either globar or halogen source with the beam passing multiple times through the cell. In these experiments, light entering the FTS had traversed the cell eight times.

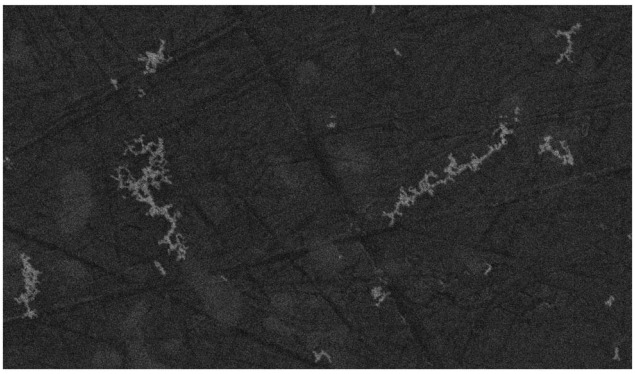

Figure 4. An example SEM image. The imaged stub was populated using an ESP at 1500UTC on 7 November 2013.

passing it into the cell, and the returning transmitted light was measured by a deuterated triglycine sulfate detector. In wave number space, the resolution of the FTS was 1.9 cm^{-1}. Using the globar source, a working range of approximately $2 < \lambda < 15$ μm was available. With the halogen source, this range could be extended slightly to $1 < \lambda < 15$ μm.

2.1.3. Direct Aerosol Measurements

The aerosol leaving the optical cell was characterized by a number of instruments measuring aerosol properties. A filter holder could be loaded with 47 mm diameter Millipore Omnipore filters with 0.1 μm pores to collect aerosol for color analysis and weighing. Bespoke electrostatic precipitators (ESP) were used to deposit particles on stubs for scanning electron microscopy (SEM). These were built to the design of *Miller et al.* [2010] and were operated as specified in that paper. In this configuration Miller found that the measured collection efficiency was 76–94% for particles with sizes from 40 to 300 nm. Particle size was measured using an Amherst Aerosizer LD aerodynamic particle sizer, a scanning mobility particle sizer (SMPS) consisting of a Grimm 5.5-900 DMA and Grimm 5403 Ultrafine Particle Counter, and a Grimm 1.108 optical particle counter.

After leaving the aerosol cell, great care was taken in controlling the mass flows so that an accurate aerosol number concentrations within the cell during optical measurements could be estimated. So as not to overload instruments, two stages of dilution were employed (after separating some of the flow for filter deposition). First, particle load was reduced by splitting the flow between a capillary tube and a particle filter preceding a mass flow meter. Only flow coming from the capillary had aerosol in it when rejoining the second path. This led to a dilution of about 5:1 (which could be accurately inferred). The second stage of dilution used a Topas DDS-560 diluter which can be set to specific dilution values. Generally, the aim of the two-stage dilution process was to have a flow diluted by about 100:1 when it reached the particle counters.

In order to keep flow constant when not loading filters, a bypass mechanism was used whereby either valve V7 was open and V8–V9 closed or vice versa. For the ESPs, the electrical field across the capillary tube could be turned off so that particles were not precipitated onto the stubs, leaving the flow unchanged.

2.2. Conversion of SEM Images to D_f and Size Distribution

Samples deposited on conducting stubs by the ESP were subsequently analyzed using an FEI Quanta 650 scanning electron microscope (SEM). The instrument was capable of rastering multiple SEM images into a large composite. This gave the opportunity to inspect magnified individual particles and to use image analysis software to build up statistics of the deposited particles. An example section of an image is shown in Figure 4.

Assuming that deposited BC aerosols were fractal aggregates (which inspection of SEM images confirmed), then using (4), the mean fractal dimension, D_f, for the deposited particles could be obtained by a linear fitting of A_a against F_{mm}. These two values were obtained by automatic image analysis using the ImageJ software package (http://imagej.nih.gov/ij).

The factor α in equation (4) was estimated empirically by comparing computer-generated fractals projected into 2-D images against the known properties of these particles. A tuneable cluster-cluster aggregation algorithm [*Thouy and Jullien*, 1994; *Filippov et al.*, 2000] was used to generate a set of 10,000 aggregates with D_f uniformly distributed between 1.4 and 2.3, and with 200 different values of n_s ranging from 100 to 1000 and a constant $k_f = 1.2$ following previous studies of light scattering by BC fractal particles [*Liu and Mishchenko*, 2005; *Zhao and Ma*, 2009; *Li et al.*, 2010]. It was found that α had a weak dependence on D_f, but since the range of actual D_f for particles formed by diffusion-limited cluster aggregation (such as BC from flames) is $D_f \simeq 1.75 \rightarrow 1.80$ [*Sorensen*, 2001], this was ignored. The value determined for α was 1.059 ± 0.035. For particles with "true" values of $D_f < 2.0$, the weak dependence of α on D_f is likely to cause a small overestimate (< 2 %) in the reported value of D_f.

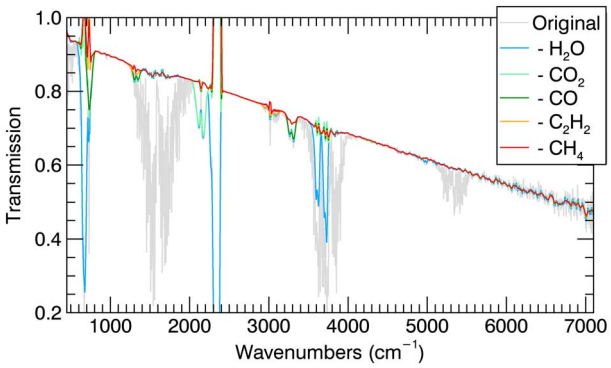

Figure 5. An example gas removal. Each overplotted spectrum represents an additional gas taken away from the transmission signal. After the final gas, CH_4, is removed, the red line shows the final transmission. This measurement is taken using the FTS with a globar source on the morning of 29 November 2013. An area of CO_2 saturation can be seen at ~2300 cm^{-1} where the transmission will be excluded due to lack of information.

Size distributions could be obtained using equation (2). Using the same technique described in the paragraph above to calculate α, k_a was found to be 1.19 ± 0.10. The projected area of individual spherules and the full particles (A_a and A_p) were obtained by inspection of the SEM image.

2.3. Conversion of FTS Measurements to MEC

2.3.1. Intensity to Transmission

Aerosol transmission, $T(\lambda)$, was obtained by measuring background spectra when the cell was empty, $E_{\text{background}}(\lambda)$, and measurement spectra when the cell was loaded $E_{\text{measurement}}(\lambda)$. This is related to the cell aerosol extinction cross section, $\sigma_e(\lambda)$:

$$\frac{E_{\text{measurement}}(\lambda)}{E_{\text{background}}(\lambda)} = T(\lambda) = e^{-N\sigma_e(\lambda)x}, \quad (6)$$

where x is the path length and N the aerosol density. The path length is a well-known quantity of the aerosol cell (3.52 m for the FTS path, 0.427 m for the grating spectrometer); N is obtained from the number counts of the SMPS, multiplied by the dilution factor from the aerosol cell exhaust to the instrument.

In practice, the background signal is obtained by measuring the cell for half an hour before aerosol enters the cell, and again at the end of the experiment when it is once again empty of aerosol. The values $E_{\text{background}}(\lambda)$ are then calculated by linear interpolation of the background signal from before and after to the time at which the measurement $E_{\text{measurement}}(\lambda)$ was taken. This is to account for any "drift" in the background signal which may have occurred due to changes in laboratory conditions. In practice, this step turned out to be unnecessary, since no measurable drift was observed between the beginning and end background signals.

Error in the measured intensity is estimated by calculating the standard deviation of intensity at each wave number for several hours before the cell is filled. This error is propagated through to transmission using standard formulae for the combination of uncertainties when multiplying measurements together. For all subsequent calculations, this propagation of uncertainties has also been applied.

2.3.2. Removal of Gas Absorption Lines

Since the burning of the fuel produces gases as well as aerosol, it is necessary to remove any gas absorption lines from the transmission measurements. We are interested in the aerosol transmission (which is unknown), so it is not possible to assume that within gas bands, the gases are the only absorbing features. Instead, the measured transmission, T, is assumed to consist of gas transmission, T_{gas} and an aerosol transmission, T_{aerosol}. The total transmission is therefore

$$T(\lambda) = T_{\text{aerosol}}(\lambda) \times T_{\text{gas}}(\lambda). \quad (7)$$

Our interest in T_{aerosol} requires us to obtain T_{gas}. The only assumption made about T_{aerosol} is that it is smoothly varying over tens of wave numbers. Thus, rapid spikes in transmission are attributed to gas interference.

The gas transmission could then be defined as the ratio of the measured transmission to the measured transmission with a boxcar smoother applied to it. Actual gas transmissions were then sequentially removed by modeling their transmission with the Reference Forward Model (http://www.atm.ox.ac.uk/RFM) and removing iteratively. Significant IR absorbers considered were H_2O, CO_2, CO, C_2H_2, and CH_4. In areas where the gas absorption lines were saturated, this still leads to problems, since there is no information about the aerosol present.

An example gas removal is shown in Figure 5. The large gas signals can be seen to leave significant residuals in the final spectrum. Since these cause an increase in the transmission error (as saturated gas signals cause large errors in T_{gas} which propagates through to T_{aerosol} at those wavelengths), they are easy to screen in the final results.

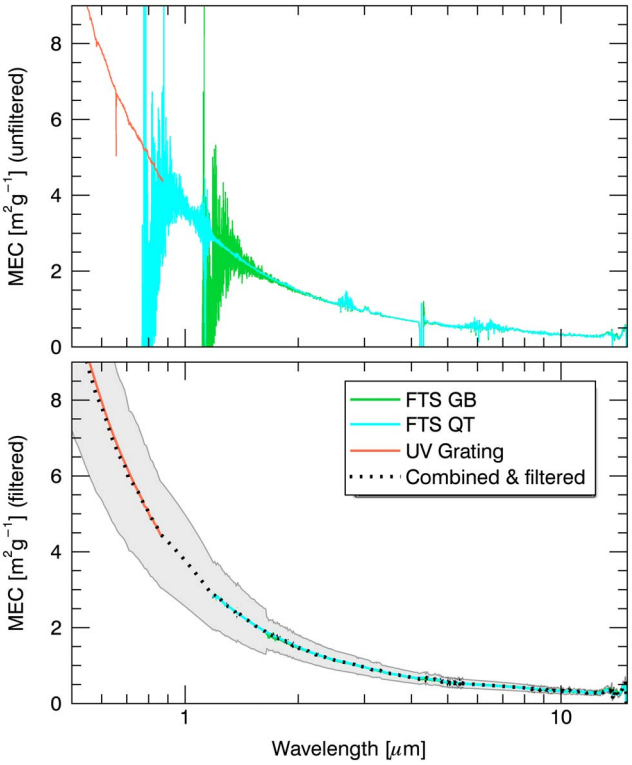

Figure 6. Calculation of MEC from the morning of 29 November 2013. (top) The unfiltered data including all three measurement instruments. (bottom) The combined MEC after bad data have been removed. Also, in Figure 6 (bottom), the grey envelope indicates the standard measurement error of the combined and filtered measurements.

2.3.3. Calculation of MEC

From the cleaned transmission measurements, T_{aerosol}, the spectral extinction, $\beta(\lambda)$ is given by

$$\beta(\lambda) = -\frac{\ln T_{\text{aerosol}}(\lambda)}{x}, \tag{8}$$

with x the path length. Single-particle extinction cross section, σ_e, was then obtained by dividing β by the particle density in the cell, N. Particle density was obtained using SMPS count data multiplied by the dilution ratio, D. The value of D was calculated using accurate and well-calibrated flow meters. As such, the largest cause of dilution uncertainty was variation in dilution throughout the experiment which lead to an average dilution uncertainty of ~4%. Assuming a black carbon density of $\rho_{\text{BC}} = 1.8$ g cm^{-3} [*Bond and Bergstrom*, 2006] and integrating over the whole range of a lognormal number distribution, the mass of an average single particle was estimated as

$$m_{\text{BC}} = \frac{4}{3}\pi r_m^3 e^{\frac{9}{2}\ln^2 S}\rho_{\text{BC}}, \tag{9}$$

where r_m and S are obtained from the SMPS lognormal fits assuming spherical particles and are the median radius and standard deviation, respectively. Finally, MEC is obtained as

$$\text{MEC}(\lambda) = \frac{\beta(\lambda)}{D N_{\text{SMPS}} m_{\text{BC}}}. \tag{10}$$

We can be sure that multiple scattering was not an issue during these experiments due to the low optical depths in the cell. Total optical depths were always less than unity outside of gas absorption features.

In Figure 6, the final MEC is shown for the same measurements made in Figure 5, with and without quality control applied to the data. Quality control consisted first of removing areas of the spectrum when the relative error in the measurement was greater than 5%. This was followed by removing spikes in the data, and finally removing areas with visible gas absorption lines still present which could not be satisfactorily removed by the gas absorption lines procedure outlined above.

3. Results

3.1. Particle Microphysical Properties

Figure 7 shows the size distributions of burnt material measured by SMPS and compared with SEM fits where available (as described in section 2.2). Qualitative agreement between the reported distributions is generally good, particularly at larger particle sizes. Quantitatively, the estimated mean volume of single BC particles (the values shown in the bottom right of each subplot) calculated from the Gaussian fit to SMPS measurements differ from the SEM measurements by a relative RMS difference of 28% and a mean difference of 17%. Much of the error in these differences can be accounted for by the abrupt cutoff in SEM-fitted measurements. This can be explained by slightly poorer focusing of the electron beam in some images, such that smaller particles were not detected by the image analysis software leading to an overestimation of mean particle volume in some SEM images.

As such, we would say that mobility sizing presents a reasonable estimation of the radius of gyration. Generally, differences between the SEM values and the SMPS values were significant. Due to concerns about

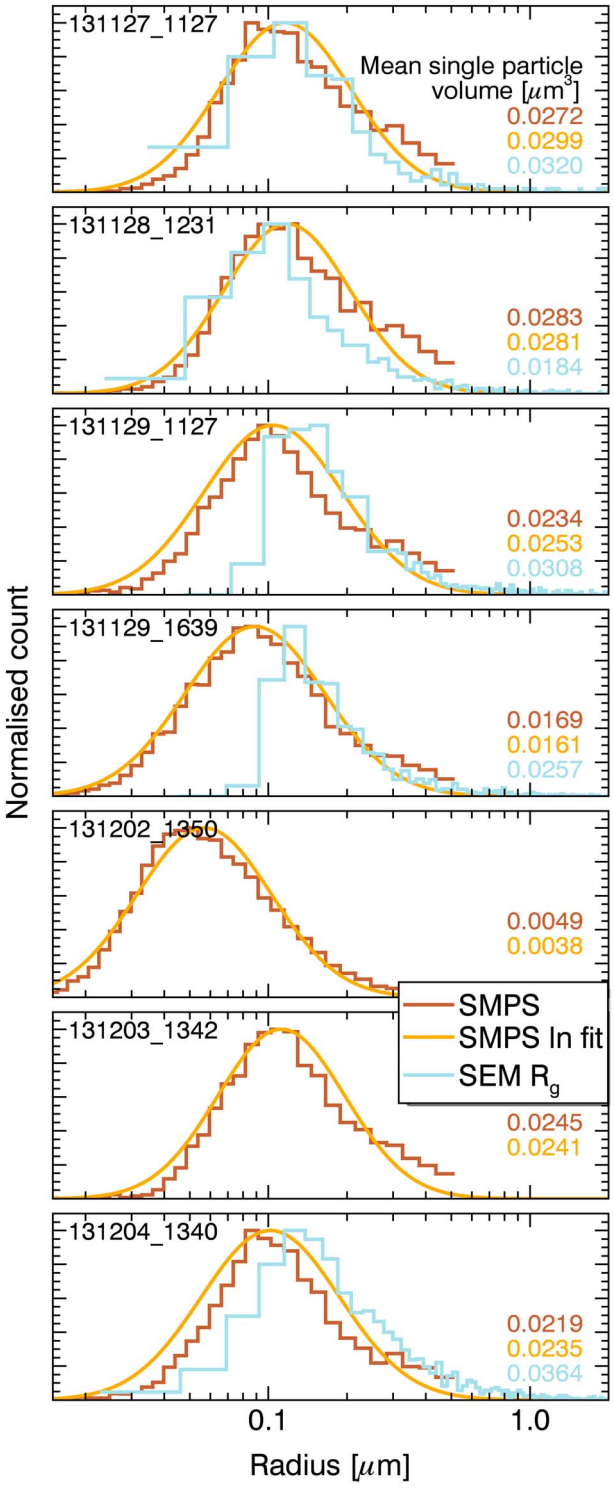

Figure 7. Size distributions measured by the SMPS and analysis of SEM images (where available). Lognormal fits to SMPS measurements are also shown to demonstrate that they are reasonable approximations to the size distribution.

the lower cutoff of the SEM data discussed above, the SMPS values were used to obtain the mass of BC in subsequent calculations. The lognormal fit to the data was chosen instead of the raw data.

Table 1 shows the microphysical data obtained from SMPS measurements, flow meters, and SEM image analysis. These data have been sorted by C/O ratio of the Mini-CAST burn. Because optical measurements were coadded to reduce the noise in the aerosol transmission, longer measurement times were preferred. This is traded off against the resultant additional noise added to the final MEC values caused by greater uncertainty in the dilution ratio of the aerosol cell to the counting instruments as this was prone to greater fluctuations over time than the aerosol cell measurements.

With an increase in C/O ratio, the mode radius of the particles decreases, in agreement with *Moore et al.* [2014] who observed the same trend for C/O> 0.35 as the flame becomes more and more fuel rich. *Schnaiter et al.* [2006] found mobility median diameters of "between 300 nm and 340 nm for the C/O ratios 0.25 and 0.29" and "less than 40 nm" at a C/O ratio of 1. If a linear relationship between the diameters and C/O ratio is assumed, the radii measured in this work are around 25 nm less. The smaller sizes observed are probably due to the shorter cell residence times in this work. While *Schnaiter et al.* [2006] waited for the initial concentration of aerosol in their cell to drop below 7×10^4 cm^{-3} through particle coagulation before beginning measurements, our cell had a constant turnover of particles as more aerosol entered through valve V1 in Figure 1 and was drawn out through valve V4. The residence time in the cell was around 25 min.

3.2. Gas Concentration Changes

The removal of gas absorption lines from the transmission measurements as described in section 2.3.2 provides the opportunity to quantitatively measure other products of the burning process since modeling the gas absorption lines requires knowledge of their concentration within the cell. Table 2 and Figure 8 show the concentration differences required to remove gas signals from the transmission measurements. As the C/O ratio increases and the mixture becomes more fuel rich, the concentration of incomplete combustion products, CO, C_2H_2, and

Table 1. Aerosol Microphysical Data Used to Obtain the Aerosol Cell Mass Loading[a]

Time Stamp	C/O Ratio	D_f	Dilution Ratio	Particle No. (cm^{-3})	r_m (μm)	S	Mean Particle Volume (μm^3)
2013/11/27 11:27	0.349	1.84	94.3 ± 2.2	26,000 ± 3,000	115 ± 0.8	1.76 ± 0.04	0.0271 ± 0.0029
2013/11/28 12:31	0.401	1.85	101.3 ± 4.5	23,500 ± 2,700	117 ± 1.9	1.75 ± 0.01	0.0271 ± 0.0009
2013/12/03 13:42	0.401	-	92.6 ± 3.8	24,600 ± 4,800	112 ± 3.4	1.74 ± 0.02	0.0231 ± 0.0012
2013/11/29 11:27	0.452	1.85	90.1 ± 4.7	22,800 ± 4,900	103 ± 2.5	1.86 ± 0.10	0.0261 ± 0.0058
2013/12/04 13:40	0.452	1.82	89.6 ± 7.2	23,800 ± 2,700	101 ± 2.9	1.80 ± 0.03	0.0206 ± 0.0018
2013/11/29 16:39	0.500	1.88	81.8 ± 1.9	32,100 ± 1,900	88 ± 1.4	1.87 ± 0.05	0.0163 ± 0.0017
2013/12/02 13:50	0.614	-	85.3 ± 0.0	48,200 ± 600	57 ± 0.3	1.82 ± 0.02	0.0039 ± 0.0002

[a]Missing D_f data are due to damaged samples which could not be analyzed.

CH_4 rises. Simultaneously, the concentration of complete combustion products, CO_2 and H_2O, decreases. The signal for water vapor is less clear than for the other gases, probably as a result of variations in humidity within the cell.

Combining the carbon mass from each of the gases, as well as from the aerosol mass (assuming a density of 1.8 g cm^{-3} entirely consisting of elemental carbon), it is not possible to take account of all of the carbon burnt. This is shown in Figure 9. Possible reasons for this could be failure to measure gases which do not have distinct absorption features in the region of interest and so were not removed from the transmission spectra (e.g., C_2H_2 which overlaps with the water vapor continuum); saturated gas absorption lines leading to underestimates in gas quantities; and extremely small, undetected black carbon and organic carbon aerosol particles being produced in greater numbers at higher C/O ratios and being too small for detection by the SMPS.

3.3. Extinction

Table 3 shows the mass extinction cross section of BC aerosol organized by the C/O ratio. Data collected on 2 December 2013 were not usable in the IR due to insufficient particulate absorption in the aerosol cell, resulting in transmissions close to unity. From Table 1, it can be seen that this is probably due to the much smaller particle size in this experiment. Visible data were still possible because of the far greater absorption of BC at shorter wavelengths.

Averaging all of the measurements provides a final MEC value at 550 nm of 8.3 ± 1.6 m^2 g^{-1}. Assuming a reasonable single scatter albedo of $\omega_0 \sim 0.2$ (in the middle of values collated by *Bond and Bergstrom* [2006]), this would lead to a mass absorption cross section of 6.6 ± 1.3 m^2 g^{-1}. This is low compared to the literature review by *Bond and Bergstrom* [2006] who presented an estimate of 7.5 ± 1.2 m^2 g^{-1}, although the values would agree within the uncertainty.

There appears to be a slight positive trend in the visible MEC as a function of the C/O ratio of the fuel mixture (see Figure 10). This might be expected since

1. $MAC_{550\,nm}$ is relatively constant as a function of size with the exception of the smallest particles [*Smith and Grainger*, 2014].
2. In Table 1, it is shown that as C/O increases, r_m decreases.

Table 2. Concentrations of Gases Required to Remove Contamination From Transmission Measurements

Time Stamp	C/O Ratio	Gas Concentration Difference Versus Background (ppmv)				
		H_2O	CO_2	CO	C_2H_2	CH_4
2013/11/27 11:27	0.349	4664.5 ± 3.4	3713.7 ± 4.2	51.1 ± 1.0	0.2 ± 0.1	0.6 ± 0.3
2013/11/28 12:31	0.401	4141.6 ± 6.6	3039.6 ± 7.6	225.8 ± 2.6	10.2 ± 0.1	2.4 ± 0.5
2013/12/03 13:42	0.401	5091.1 ± 3.3	3563.3 ± 4.2	264.7 ± 1.8	12.6 ± 0.1	3.0 ± 0.3
2013/11/29 11:27	0.452	4734.5 ± 4.4	2997.3 ± 5.1	460.7 ± 3.9	66.5 ± 0.8	33.7 ± 0.4
2013/12/04 13:40	0.452	5009.5 ± 2.8	3143.5 ± 3.1	483.0 ± 2.5	67.2 ± 0.5	34.3 ± 0.2
2013/11/29 16:39	0.500	4218.6 ± 3.2	2464.2 ± 3.6	476.2 ± 3.2	99.1 ± 1.1	69.3 ± 0.3
2013/12/02 13:50	0.614	4388.2 ± 2.9	2523.4 ± 2.6	514.8 ± 3.1	145.1 ± 1.6	177.8 ± 0.4

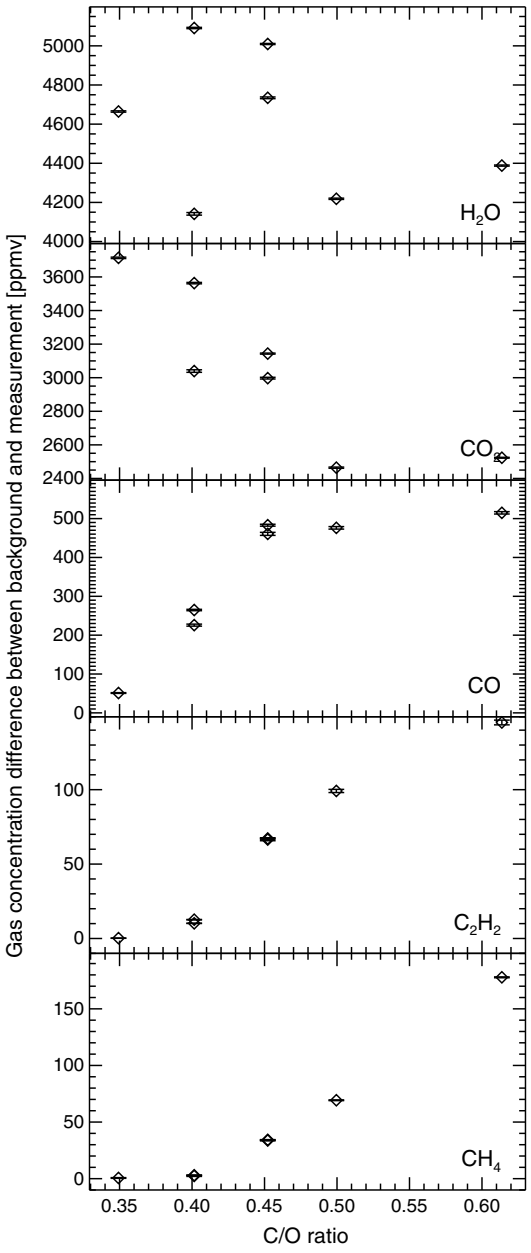

Figure 8. The increase in gas concentrations in the aerosol cell between background and measurements.

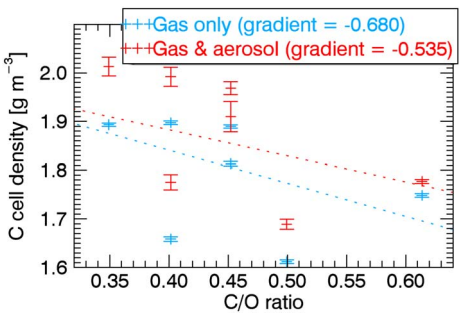

Figure 9. Estimated cell carbon density increase during experiments as a function of the C/O ratio.

Using the single scatter albedo and MAC from Table 1 of *Schnaiter et al.* [2006], we can calculate their values of MEC at 550 nm. Doing this, we find a negative trend in extinction as a function of C/O, contrary to our findings. As discussed in section 3.1, different sizes of particles were obtained in our two methods with the radii being smaller in this work. Reducing the sizes of the median radii such that they match the sizes reported by *Schnaiter et al.* [2006] while holding all other values constant leads to a reversal of the trend reported in Figure 10. This is because the 25 nm change in radius for smaller particles has a much larger effect on the mean particle volume than for the larger particles at lower C/O ratios. In the IR at all wavelengths, MEC decreases as a function of C/O, due to decreasing absorption efficiency at smaller particle sizes. This is also shown in Figure 10.

The measurement at C/O = 0.35 seems abnormally low at all wavelengths, compared to rest of the experiments, and we are not confident that this data point is not an aberration. At all measurement points in our experiments, we have a fuel mix that is fuel rich and so we cannot think of a physical reason that there would be such a drop in MEC in this case, especially since other works do not see this result. As such we would caution readers about the data with C/O = 0.35.

At larger C/O ratios, the organic carbon content of the aerosols is increased [*Schnaiter et al.*, 2006; *Moore et al.*, 2014], likely in the form of condensed polyaromatic hydrocarbons. When C/O ratios are > 0.4, it is likely that OC is a significant presence in extinction measurements. The effect of this would be either to enhance absorption, by forming a coating on the BC leading to lensing of light [*Bond et al.*, 2006], or to lower the absorption by internally or externally mixing a less absorbing aerosol in with the strongly absorbing BC. Given the lack of visible coating on BCFAs viewed in SEM images, it is likely that unquantified OC content would cause the MEC values provided here to be underestimated, particularly at larger C/O ratios.

3.4. The Ångström Exponent

The extinction Ångström exponent, α_e, is used at visible and NIR wavelengths as a rough method of distinguishing between fine- and coarse-mode aerosol particles in the atmosphere. Values of $\alpha_e \geq 2$ suggest finer, more absorbing particles such as urban, industrial, and biomass burning aerosols [*Eck et al.*, 1999]. Values of $\alpha_e \leq 1$ suggest aerosols dominated by

Table 3. Spectral MEC Values[a]

Time Stamp	C/O Ratio	Mass Extinction Cross Section ($m^2\ g^{-1}$) 550 nm	2 μm	4 μm	6 μm	8 μm	12 μm
2013/11/27 11:27	0.349	5.44 ± 0.87	1.35 ± 0.15	0.71 ± 0.08	0.52 ± 0.06	0.43 ± 0.05	0.28 ± 0.03
2013/11/28 12:31	0.401	6.96 ± 0.89	1.58 ± 0.14	0.81 ± 0.07	0.59 ± 0.05	0.50 ± 0.05	0.34 ± 0.03
2013/12/03 13:42	0.401	9.71 ± 2.00	2.25 ± 0.33	1.15 ± 0.17	0.84 ± 0.12	0.69 ± 0.10	0.48 ± 0.07
2013/11/29 11:27	0.452	8.95 ± 2.81	1.47 ± 0.33	0.69 ± 0.15	0.50 ± 0.11	0.41 ± 0.09	0.28 ± 0.06
2013/12/04 13:40	0.452	10.59 ± 1.73	1.89 ± 0.22	0.87 ± 0.10	0.63 ± 0.07	0.52 ± 0.06	0.37 ± 0.04
2013/11/29 16:39	0.500	7.84 ± 0.97	0.94 ± 0.08	0.40 ± 0.03	0.30 ± 0.03	0.24 ± 0.02	0.17 ± 0.02
2013/12/02 13:50	0.614	8.67 ± 0.43	-	-	-	-	-
	Mean	8.31 ± 1.59	1.58 ± 0.23	0.77 ± 0.11	0.56 ± 0.08	0.46 ± 0.07	0.32 ± 0.05

[a]Missing MEC data are due to insignificant aerosol in the cell to provide aerosol extinction.

coarse-mode particles, such as desert dust and maritime aerosol [*Schuster et al.*, 2006]. By fitting a straight line to the logarithm of extinction as a function of the logarithm of wavelength, one obtains α_e as the negative gradient [*Ångström*, 1929]:

$$\beta(\lambda) = \beta_0 \times \lambda^{-\alpha_e}. \tag{11}$$

More generally, one can obtain the general extinction Ångström coefficient, EAC(λ), by calculating the slope between two extinction measurements as a function of λ on a log-log plot [*Moosmüller and Chakrabarty*, 2011]. For this work, it was found that the EAC varied with wavelength, increasing from a value of 1 at short wavelengths, peaking at around 700 nm with EAC $\simeq$ 1.6 and then decreasing though the NIR to settle at a value of around 0.82±0.05 in the thermal IR. This spectrally dependent EAC suggested that a single-Ångström exponent was not suitable, and so the additional "curvature," c, of the exponent was also calculated following *Schuster et al.* [2006], by adding a squared ln λ term:

$$\ln \beta(\lambda) = \ln \beta_0 - \alpha_e \ln \lambda + c \ln^2 \lambda, \tag{12}$$

and only fitting the polynomial in the range up to $\lambda = 2$ μm.

The results of these fits as a function of the C/O ratio are shown in Figure 11. First, we note that the α_e is smaller than might be expected, with a value of $\alpha_e = 1.3 \pm 0.2$. Since we are mainly looking at particles with SMPS measured mode radii of ~0.1 μm, we might have expected a value much closer to 2. However, these larger values of α_e were reported for atmospheric aerosols, not fresh BC. Additionally, for spectral regions with a constant imaginary refractive index and particles small relative to the wavelength, the absorption Ångström coefficient α_a is expected to be close to unity [*Bohren and Huffman*, 1983]. Given that the single scatter albedo is expected to be small, we expect $\alpha_a \approx \alpha_e$ [*Moosmüller and Chakrabarty*, 2011].

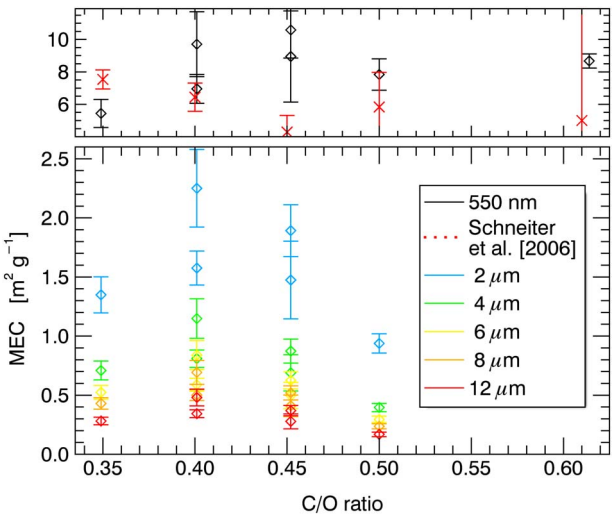

Figure 10. Mass extinction cross section as a function of burning C/O ratio at selected wavelengths. At 550 nm, the extinction obtained from *Schnaiter et al.* [2006] is also shown.

The curvature is negative with a mean value of $c = -0.22 \pm 0.04$. Negative curvatures are reported to be a sign of increased fine-mode fraction in monomodal aerosol distributions [*Schuster et al.*, 2006]. Additionally, as the C/O ratio increases (and the size of particles decreases), we notice an

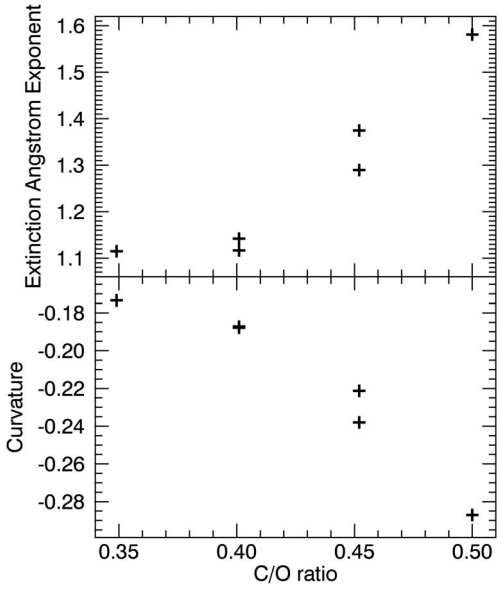

Figure 11. The extinction Ångström exponent and associated curvature, as a function of the C/O ratio fitted for data with $\lambda < 2$ μm.

increase in α_e and a decrease in c (becoming even more negative), both of which are symptomatic of an increased fine-mode fraction. There was no C/O dependence of the Ångström exponent in the thermal IR.

3.5. Fractal Dimension

The fitted fractal observations also shown in Table 1 have a mean value of 1.85 ± 0.02. This is slightly higher than literature values for burning flames which are generally said to be $1.7 < D_f < 1.8$ [*Sorensen*, 2001]. The width of the 95% confidence interval for individual measurements was 0.11. The likely slight overestimate due to the D_f dependence of α is not large enough to bring our reported mean value of D_f into agreement with the range reported by *Sorensen* [2001]. No trend in D_f as a function of the flame C/O ratio was observed. The fractal nature of the particles observed shows that measurements made in this experiment were of very "fresh" BC.

4. Conclusions

This work has presented measurements of fresh black carbon aerosol mass extinction cross sections using Fourier transform infrared and optical spectroscopy. MEC values are used to calculate optical depths from model results, which can be directly tested by ground- and satellite-based measurements. The values of extinction suggest absorption cross sections slightly lower than those found in the current literature, but within error bars.A further unquantified source of error in this experiment is the role of organic carbon content, likely causing the MEC values to be underestimated at higher C/O ratios.

Future work will provide retrieval of the cell transmission data using a band model in an attempt to obtain refractive index and light scattering properties of the aerosol. This should enable the direct calculation of MAC in the visible as a derived retrieval product. In the IR, our MEC values are a suitable substitute for MAC due to the low scattering cross sections.

Acknowledgments
All data presented in section 3 can be obtained from the corresponding author (smith@atm.ox.ac.uk) on request. This work was supported by the Natural Environmental Research Council (grant NE/F018142/1). The Rutherford Appleton Laboratory Molecular Spectroscopy Facility is supported by the Natural Environmental Research Council. We thank Gary Williams from the Rutherford Appleton Laboratory for his assistance in making these measurements.

References

Ångström, A. (1929), On the atmospheric transmission of Sun radiation and on dust in the air, *Geogr. Ann.*, *11*, 156–166, doi:10.2307/519399.
Bahadur, R., Y. Feng, L. M. Russell, and V. Ramanathan (2011), Impact of California's air pollution laws on black carbon and their implications for direct radiative forcing, *Atmos. Environ.*, *45*(5), 1162–1167, doi:10.1016/j.atmosenv.2010.10.054.
Bohren, C. F., and D. R. Huffman (1983), *Absorption and Scattering of Light by Small Particles*, Wiley–VCH, Weinheim, Germany, doi:10.1002/9783527618156.
Bond, T. C. (2007), Can warming particles enter global climate discussions?, *Environ. Res. Lett.*, *2*(4), 045030, doi:10.1088/1748-9326/2/4/045030.
Bond, T. C., and R. W. Bergstrom (2006), Light absorption by carbonaceous particles: An investigative review, *Aerosol Sci. Technol.*, *40*(1), 27–67, doi:10.1080/02786820500421521.
Bond, T. C., G. Habib, and R. W. Bergstrom (2006), Limitations in the enhancement of visible light absorption due to mixing state, *J. Geophys. Res.*, *111*, D20211, doi:10.1029/2006JD007315.
Bond, T. C., E. Bhardwaj, R. Dong, R. Jogani, S. Jung, C. Roden, D. G. Streets, and N. M. Trautmann (2007), Historical emissions of black and organic carbon aerosol from energy-related combustion, 1850–2000, *Global Biogeochem. Cycles*, *21*, GB2018, doi:10.1029/2006GB002840.
Bond, T. C., et al. (2013), Bounding the role of black carbon in the climate system: A scientific assessment, *J. Geophys. Res. Atmos.*, *118*, 5380–5552, doi:10.1002/jgrd.50171.
Calcote, H. F. (1981), Mechanisms of soot nucleation in flames—A critical review, *Combust. Flame*, *42*, 215–242, doi:10.1016/0010-2180(81)90159-0.
Doherty, S. J., S. G. Warren, T. C. Grenfell, A. D. Clarke, and R. E. Brandt (2010), Light-absorbing impurities in Arctic snow, *Atmos. Chem. Phys.*, *10*(23), 11,647–11,680, doi:10.5194/acp-10-11647-2010.
Eck, T. F., B. N. Holben, J. S. Reid, O. Dubovik, A. Smirnov, N. T. O'Neill, I. Slutsker, and S. Kinne (1999), Wavelength dependence of the optical depth of biomass burning, urban, and desert dust aerosols, *J. Geophys. Res.*, *104*(D24), 31,333–31,349, doi:10.1029/1999JD900923.
Filippov, A. V., M. Zurita, and D. E. Rosner (2000), Fractal-like aggregates: Relation between morphology and physical properties, *J. Colloid Interface Sci.*, *229*(1), 261–273, doi:10.1006/jcis.2000.7027.

Flanner, M. G., C. S. Zender, P. G. Hess, N. M. Mahowald, T. H. Painter, V. Ramanathan, and P. J. Rasch (2009), Springtime warming and reduced snow cover from carbonaceous particles, *Atmos. Chem. Phys.*, *9*(7), 2481–2497, doi:10.5194/acp-9-2481-2009.

Fuller, K. A., W. C. Malm, and S. M. Kreidenweis (1999), Effects of mixing on extinction by carbonaceous particles, *J. Geophys. Res.*, *104*(D13), 15,941–15,954, doi:10.1029/1998JD100069.

Hansen, J., M. Sato, and R. Ruedy (1997), Radiative forcing and climate response, *J. Geophys. Res.*, *102*(D6), 6831–6864, doi:10.1029/96JD03436.

Intergovernmental Panel on Climate Change (IPCC) (2013), *Climate Change 2013: The Physical Science Basis. Contribution of Working Group I to the Fifth Assessment Report of the Intergovernmental Panel on Climate Change*, 1535 pp., Cambridge Univ. Press, Cambridge, U. K., and New York.

Ito, A., and J. E. Penner (2005), Historical emissions of carbonaceous aerosols from biomass and fossil fuel burning for the period 1870–2000, *Global Biogeochem. Cycles*, *19*, GB2028, doi:10.1029/2004GB002374.

Jacobson, M. Z. (2001), Strong radiative heating due to the mixing state of black carbon in atmospheric aerosols, *Nature*, *409*(6821), 695–697, doi:10.1038/35055518.

Jansen, K. L., T. V. Larson, J. Q. Koenig, T. F. Mar, C. Fields, J. Stewart, and M. Lippmann (2005), Associations between health effects and particulate matter and black carbon in subjects with respiratory disease, *Environ. Health Perspect.*, *113*(12), 1741–1746, doi:10.1289/ehp.8153.

Köylü, U. O., and G. M. Faeth (1992), Structure of overfire soot in buoyant turbulent diffusion flames at long residence times, *Combust. Flame*, *89*(2), 140–156, doi:10.1016/0010-2180(92)90024-J.

Köylü, U. O., G. M. Faeth, T. L. Farias, and M. G. Carvalho (1995), Fractal and projected structure properties of soot aggregates, *Combust. Flame*, *100*(4), 621–633, doi:10.1016/0010-2180(94)00147-K.

Larson, S. M., G. R. Cass, and H. A. Gray (1989), Atmospheric carbon particles and the Los Angeles visibility problem, *Aerosol Sci. Technol.*, *10*(1), 118–130, doi:10.1080/02786828908959227.

Li, H., C. Liu, L. Bi, P. Yang, and G. W. Kattawar (2010), Numerical accuracy of "equivalent" spherical approximations for computing ensemble-averaged scattering properties of fractal soot aggregates, *J. Quant. Spectrosc. Radiat. Transfer*, *111*(14), 2127–2132, doi:10.1016/j.jqsrt.2010.05.009.

Liu, L., and M. I. Mishchenko (2005), Effects of aggregation on scattering and radiative properties of soot aerosols, *J. Geophys. Res.*, *110*, D11211, doi:10.1029/2004JD005649.

Martins, J. V., P. Artaxo, C. Liousse, J. S. Reid, P. V. Hobbs, and Y. J. Kaufman (1998a), Effects of black carbon content, particle size, and mixing on light absorption by aerosols from biomass burning in Brazil, *J. Geophys. Res.*, *103*(D24), 32,041–32,050, doi:10.1029/98JD02593.

Martins, J. V., P. V. Hobbs, R. E. Weiss, and P. Artaxo (1998b), Sphericity and morphology of smoke particles from biomass burning in Brazil, *J. Geophys. Res.*, *103*(D24), 32,051–32,057, doi:10.1029/98JD01153.

Miller, A., G. Frey, G. King, and C. Sunderman (2010), A handheld electrostatic precipitator for sampling airborne particles and nanoparticles, *Aerosol Sci. Technol.*, *44*(6), 417–427, doi:10.1080/02786821003692063.

Moore, R. H., L. D. Ziemba, D. Dutcher, A. J. Beyersdorf, K. Chan, S. Crumeyrolle, T. M. Raymond, K. L. Thornhill, E. L. Winstead, and B. E. Anderson (2014), Mapping the operation of the Miniature Combustion Aerosol Standard (Mini-CAST) soot generator, *Aerosol Sci. Technol.*, *48*(5), 467–479, doi:10.1080/02786826.2014.890694.

Moosmüller, H., and R. K. Chakrabarty (2011), Technical Note: Simple analytical relationships between Ångström coefficients of aerosol extinction, scattering, absorption, and single scattering albedo, *Atmos. Chem. Phys.*, *11*(20), 10,677–10,680, doi:10.5194/acp-11-10677-2011.

Moosmüller, H., R. K. Chakrabarty, and W. P. Arnott (2009), Aerosol light absorption and its measurement: A review, *J. Quant. Spectrosc. Radiat. Transfer*, *110*(11), 844–878, doi:10.1016/j.jqsrt.2009.02.035.

Popovicheva, O., N. M. Persiantseva, N. K. Shonija, P. DeMott, K. Koehler, M. Petters, S. Kreidenweis, V. Tishkova, B. Demirdjian, and J. Suzanne (2008), Water interaction with hydrophobic and hydrophilic soot particles, *Phys. Chem. Chem. Phys.*, *10*, 2332–2344, doi:10.1039/b718944n.

Schnaiter, M., M. Gimmler, I. Llamas, C. Linke, C. Jäger, and H. Mutschke (2006), Strong spectral dependence of light absorption by organic carbon particles formed by propane combustion, *Atmos. Chem. Phys.*, *6*(10), 2981–2990, doi:10.5194/acp-6-2981-2006.

Schuster, G. L., O. Dubovik, and B. N. Holben (2006), Angstrom exponent and bimodal aerosol size distributions, *J. Geophys. Res.*, *111*, D07207, doi:10.1029/2005JD006328.

Smith, A. J. A., and R. G. Grainger (2014), Simplifying the calculation of light scattering properties for black carbon fractal aggregates, *Atmos. Chem. Phys.*, *14*(15), 7825–7836, doi:10.5194/acp-14-7825-2014.

Sorensen, C. M. (2001), Light scattering by fractal aggregates: A review, *Aerosol Sci. Technol.*, *35*(2), 648–687, doi:10.1080/02786820117868.

Su, D. S., J.-O. Müller, R. E. Jentoft, D. Rothe, E. Jacob, and R. Schlögl (2004), Fullerene-like soot from EuroIV diesel engine: Consequences for catalytic automotive pollution control, *Top. Catal.*, *30–31*, 241–245, doi:10.1023/B:TOCA.0000029756.50941.02.

Thomas, G. E., S. F. Bass, R. G. Grainger, and A. Lambert (2005), Retrieval of aerosol refractive index from extinction spectra with a damped harmonic-oscillator band model, *Appl. Opt.*, *44*(7), 1332–1341, doi:10.1364/AO.44.001332.

Thouy, R., and R. Jullien (1994), A cluster-cluster aggregation model with tunable fractal dimension, *J. Phys. A: Math. Gen.*, *27*(9), 2953, doi:10.1088/0305-4470/27/9/012.

Vander Wal, R. L., T. M. Ticich, and A. B. Stephens (1999), Can soot primary particle size be determined using laser-induced incandescence?, *Combust. Flame*, *116*(1–2), 291–296, doi:10.1016/S0010-2180(98)00040-6.

Wagner, H. Gg. (1981), Soot formation—An overview, in *Particulate Carbon: Formation During Combustion*, edited by D. C. Siegla and G. W. Smith, pp. 1–29, Springer, doi:10.1007/978-1-4757-6137-5_1.

Zhang, R., A. F. Khalizov, J. Pagels, D. Zhang, H. Xue, and P. H. McMurry (2008), Variability in morphology, hygroscopicity, and optical properties of soot aerosols during atmospheric processing, *Proc. Natl. Acad. Sci. U.S.A.*, *105*(30), 10,291–10,296, doi:10.1073/pnas.0804860105.

Zhao, Y., and L. Ma (2009), Applicable range of the Rayleigh-Debye-Gans theory for calculating the scattering matrix of soot aggregates, *Appl. Opt.*, *48*(3), 591–597, doi:10.1364/AO.48.000591.